Nanoporous pyropolymer nanosheets fabricated from renewable bio-resources for supercapacitors

CrossMark

Jaewon Choi [a,†], Na Rae Kim [b,†], Hyoung-Joon Jin [b,*], Young Soo Yun [c,*]

[a] Department of Materials Science and Engineering, University of Illinois at Urbana–Champaign, Urbana, IL 61801, United States
[b] Department of Polymer Science and Engineering, Inha University, Incheon 402-751, South Korea
[c] Department of Chemical Engineering, Kangwon National University, Samcheok 245-711, South Korea

A B S T R A C T

In this study, nanoporous pyropolymer nanosheets (NPNs) were fabricated from Citreae peels by simple pyrolysis with potassium hydroxide. The NPNs have a high specific surface area of $1522\ m^2\ g^{-1}$, numerous nanometer-scale pores, a high electrical conductivity of $210\ S\ cm^{-1}$, and a large amount of oxygen (19.4 wt.%) and nitrogen (3.4 wt.%) heteroatoms. These unique material properties lead to good electrochemical performance of NPNs as supercapacitor electrodes; they showed high specific capacitance of $330\ F\ g^{-1}$, good rate capabilities ($221\ F\ g^{-1}$ to $60\ A\ g^{-1}$), and stable cyclic performance for more than 20,000 cycles. This study provides information on the simple fabrication of sustainable and functional carbon-based materials containing numerous nanopores and redox-active heteroatoms. In addition, these materials demonstrate superior electrochemical performances as electrodes for supercapacitors.

© 2016 The Korean Society of Industrial and Engineering Chemistry. Published by Elsevier B.V. All rights reserved.

Introduction

With the rapid advancement of modern electronics and an increasing demand for electric vehicles, energy storage devices having high electrochemical performances have attracted significant attention [1–3]. Electrochemical double layer (EDL) capacitors, known as supercapacitors, can supply high power owing to their rapid charge storage characteristics [1–3]. However, the low-energy character of supercapacitors greatly limits their integration into state-of-the-art electronic devices [1,2]. One of the key factors for increasing the energy density of supercapacitors is the development of advanced electrode materials with high surface area and effective EDL thickness [4–20]. Xia et al. reported hierarchical porous carbons with a high specific surface area of $2749\ m^2\ g^{-1}$ and a specific capacitance of $223\ F\ g^{-1}$ in a 6 M KOH electrolyte [7]. Béguin et al. reported that activated carbon with a high surface area of $3030\ m^2\ g^{-1}$ showed a capacitance of $260\ F\ g^{-1}$ [9]. More recently, Sun et al. prepared porous carbons with a higher specific surface area of $3175\ m^2\ g^{-1}$ and a correspondingly higher specific capacitance of $\sim275\ F\ g^{-1}$ [20]. These reports highlight the

importance of large active surface areas in capacitive charge storage. However, there is a difference between the electrochemically active surface area and the measured Brunauer–Emmett–Teller (BET) specific surface area. Yun et al. have demonstrated the discordance between electrochemical performances and specific surface areas [18]. Additionally, the nanostructure, textural properties, and surface functional groups affect the charge storage behaviors of supercapacitors. Wang et al. reported that three-dimensional low-layer graphene/multi-walled carbon nanotube hybrid nanostructures exhibit a high specific capacitance of $286\ F\ g^{-1}$ [19]. Mesoporous carbon hollow spheres with large tunable pore sizes allow for the specific capacitance to be increased to $\sim310\ F\ g^{-1}$ [21]. Moreover, pseudocapacitive charge storage behaviors on the surface redox-active heteroatoms of carbon-based materials leads to a dramatic enhancement of charge storage capacity [4,8,22–26]. Huang et al. reported that nitrogen-enriched porous carbon nanofiber networks possessing $\sim5.44\%$ nitrogen atoms and a specific surface area of $753\ m^2\ g^{-1}$ showed a specific capacitance of $302\ F\ g^{-1}$ [22]. Thus, elaborately designed nanostructured electrode materials possessing high specific surface areas, effective pore structures, and redox-active heteroatoms are required to achieve high-energy supercapacitors.

Pyropolymers are carbonaceous materials containing numerous heteroatoms, because they are prepared by the pyrolysis of a

* Corresponding authors.
  E-mail addresses: hjjin@inha.ac.kr (H.-J. Jin), ysyun@kangwon.ac.kr (Y.S. Yun).
† These authors contributed equally to this work.

polymer precursor in a relatively low temperature range of 400–1000 °C [27]. Most thermoset polymers and cyclolinear polymers can be converted to pyropolymers by simply heating them in an inert atmosphere. Furthermore, by using a well-defined wet process in polymer science, nanostructured pyropolymers containing a large amount of redox-active heteroatoms can be readily fabricated. The advantages of a simple fabrication method and mass production can be maximized using renewable biomass as the polymer precursor.

In this study, nanoporous pyropolymer nanosheets (NPNs) containing a large amount of redox-active heteroatoms were fabricated from Citreae peels by simple pyrolysis with potassium hydroxide followed by an acid treatment. The NPNs had a two-dimensional (2D) nanostructure with a high aspect ratio (>100), a high specific surface area of 1522 m^2 g^{-1}, a hierarchical nanopore structure, and redox-active oxygen and nitrogen heteroatoms of concentrations 19.4 wt.% and 3.4 wt.%, respectively. These properties led to high electrochemical performances of the NPNs as electrodes for supercapacitors.

Experimental

Preparation of NPNs

Citreae peels were washed with deionized water and ethanol several times to remove adhered dirt and then were chopped into small pieces. The small peel pieces (100 g) were soaked in a 6 M KOH (95%, Samchun Pure Chemical Co., Ltd., Korea) aqueous solution for 1 h, and then freeze-dried using a lyophilizer at −50 °C and under 0.0045 mbar pressure for 72 h. The dried peels now containing K$^+$ ions were then pyrolyzed at 800 °C in a tube furnace under nitrogen atmosphere, using a heating rate of 10 °C min^{-1} and holding time of 2 h at the final temperature. After the one-step pyrolysis/activation process, the resulting products were treated in 30 wt.% nitric acid at 60 °C for 2 h to remove inorganic impurities and to introduce additional oxygen-containing functional groups on the surface of the NPNs. Then, the NPNs were washed using water and ethanol several times and stored in a vacuum oven at 25 °C.

Electrochemical characterization

Electrochemical measurements were performed using a three-electrode system with Ag/AgCl and Pt as the reference and counter electrodes, respectively, and a two-electrode system composed of symmetric active materials in a beaker cell. For electrode preparation, 5 wt.% polytetrafluoroethylene (PTFE, Sigma-Aldrich, 60 wt.% dispersion in H$_2$O) was added to the NPNs as a binder. Typically, the NPN samples and the PTFE were mixed using a mortar and pestle to form a paste, which was rolled into uniformly thick sheets (thicknesses of 40–50 μm), and punched into 1-cm-diameter electrodes. The electrodes weighed 3–4 mg after drying overnight at 100 °C. Aqueous solutions of 6 M KOH were used as electrolytes to investigate the electrochemical performance of the NPNs. Electrochemical data were obtained using cyclic voltammetry, chronopotentiometry, and electrical impedance spectroscopy (EIS) (PGSTAT302N, Autolab). Capacitance, energy density, and power density were all characterized by galvanostatic measurements. The specific capacitances of the symmetric supercapacitors were determined from the galvanostatic measurements using the following equation:

$$C = \frac{4I_{cons}}{m \, dv/dt},\tag{1}$$

where I_{cons} is the (constant) current, m is the total mass of both carbon electrodes, and dV/dt was calculated from the slope of the

discharge curve over the range from $V = V_{max}$ (the voltage at the beginning of discharge) to $V = V_{min}$. The specific power density and energy density of the supercapacitors were also calculated as follows:

$$P = \Delta V \times \frac{l}{m},\tag{2}$$

$$E = \frac{P \times t}{3600}, \text{ and}\tag{3}$$

$$\Delta V = \frac{E_{max} + E_{min}}{2}\tag{4}$$

In Eqs. (2)–(4), E_{max} and E_{min} are the potentials at the beginning and at the end of discharge (V), respectively, I is the charge/discharge current (A), t is the discharge time (s), and m is the total mass (kg) of the active materials, including both electrodes, in the symmetric supercapacitors.

Characterization

The morphologies of the prepared samples were examined using field-emission transmission electron microscopy (FE-TEM, JEM2100F, JEOL, Tokyo, Japan) and field-emission scanning electron microscopy (FE-SEM, S-4300, Hitachi, Tokyo, Japan). Topographical images of the samples were obtained using an atomic force microscope (Cypher, Oxford Instruments AFM Inc.) with a tapping mode cantilever. The chemical compositions of the samples were evaluated using X-ray photoelectron spectroscopy (XPS, PHI 5700 ESCA, Chanhassen, MN, USA) with monochromatic Al Kα radiation ($h\nu$ = 1486.6 eV) and elemental analysis (EA) with an EA1112 instrument (CE Instrument, Italy). X-ray diffraction (XRD, Rigaku DMAX 2500) was performed using Cu Kα radiation (with a wavelength λ = 0.154 nm) at 40 kV and 100 mA. Raman spectra were recorded using a continuous-wave linearly polarized laser with a wavelength of 514 nm, a 50-μm pinhole, and a 600-groove/mm grating. To ensure nondestructive measurements, a low laser power of <300 μW was used to irradiate the samples. In addition, the BET specific surface area and differential pore volumes were determined from nitrogen adsorption/desorption isotherms (ASAP 2020, Micromeritics, Norcross, GA, USA) at −196 °C. The electrode was fabricated by conventional electron beam lithography (15 keV acceleration voltage). Cr/Au (3/100 nm) was deposited using an electron gun evaporation system under high vacuum (<1 × 10^{-3} Pa) and lift-off procedures. Temperature-dependent I–V characteristics were determined using a conventional two-probe method with a Janis cryogenic system and semiconductor characterization system (4200-SCS, Keithley). Electrical measurements were taken after vacuum degassing for 12 h (<5 × 10^{-4} Pa).

Results and discussion

The morphologies of the NPNs are shown in Fig. 1. The NPNs had a 2D nanosheet structure with a high aspect ratio (>100), of which the lateral sizes were several micrometers [Fig. 1(a)–(c) and (e)], and the thickness was ~10 nm [Fig. 1(f)]. The NPN surfaces were very rough, suggesting that a porous structure had developed on their surface [Fig. 1(f)]. The rough surfaces of the NPNs could be induced by a two-step chemical activation of the polymeric precursors with potassium hydroxide [4,8,28]. The first step is the consumption of carbon by oxygen producing carbon monoxide and carbon dioxide, catalyzed by alkali metals below 700 °C. The second activation step occurs above 700 °C and is accompanied by the formation of metallic potassium, which penetrates into the
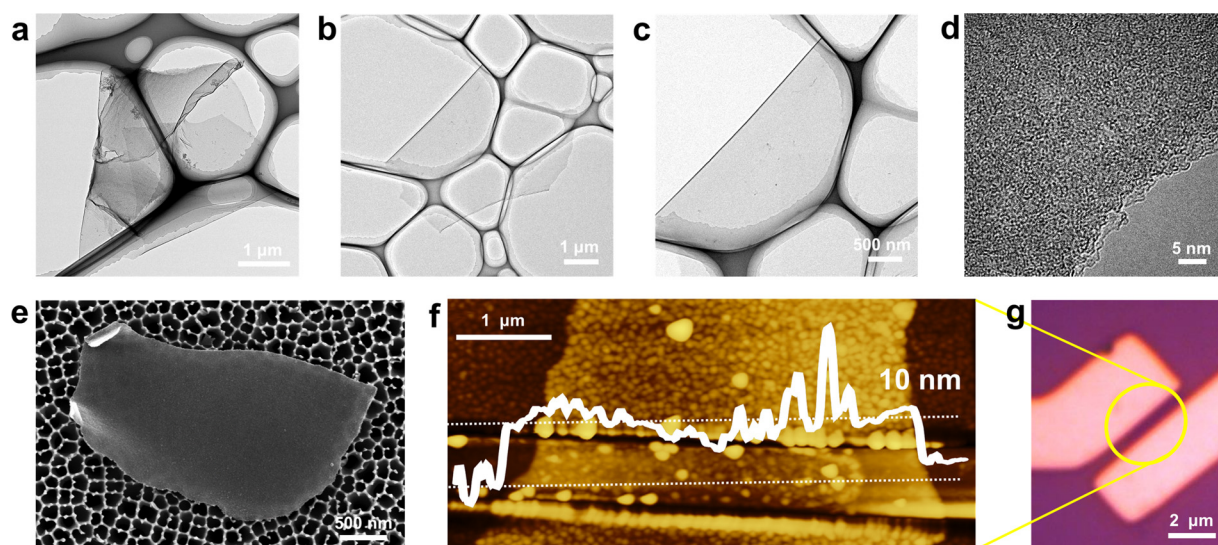
Fig. 1. (a–d) FE-TEM images at different magnifications and (e) FE-SEM image of the NPNs. (f) Topographic image of NPNs characterized by AFM and (g) an optical image of the NPNs on the two electrode configuration for characterization.

graphitic layers formed by pyrolysis and results in numerous topological defects and expansion of the graphitic lattice by rapid removal of the intercalated potassium. Many nanometer-scale pores could be induced by random aggregation of the expanded graphitic layers. The high-resolution FE-TEM image showed that there was no long-range carbon ordering, suggesting that the NPNs have an amorphous carbon structure. Further specifics regarding the carbon microstructure of the NPNs were investigated by Raman spectroscopy and XRD analysis, as shown in Fig. 2. Raman spectra of the samples show D and G bands centered at 1356 and 1580 cm^{-1}, respectively, as depicted in Fig. 2(a), which correspond to the disorder in the A$_{1g}$ breathing mode of the six-fold aromatic ring near the basal edge and the hexagonal carbon structure related to the E$_{2g}$ vibration mode of the sp^2-hybridized C atoms, respectively [11]. The I_D/I_G intensity ratio of the NPNs was 0.81, indicating that the hexagonal carbon structure was a few nanometers in size. The XRD patterns of the NPNs show the broad graphite (0 0 2) peak at 24.9° [Fig. 2(b)], indicating a poor stacking order of the hexagonal carbon structure. These data also suggest that the NPNs are composed of random aggregates of the nanometer-scale hexagonal carbon structure with numerous defect sites and edge functional groups. Therefore, the NPNs can have a large number of heteroatoms and numerous nanometer-scale pores.

Surface properties of the NPNs were characterized by XPS [Fig. 3]. In the XPS C 1s spectrum (Fig. 3(a)), the peaks corresponding to the main C–C bonding was centered at 284.3 eV, the peaks for C–O and C–N bonding were centered at 285.7 eV, and the peak for C(O)O bonding centered at 290.2 eV. In addition, two distinct peaks, namely C=O bonding and C–O bonding, were centered at 531.2 eV and 533.6 eV, respectively, were found in the XPS O 1s spectrum [Fig. 3(b)]. The chemical structure of the nitrogen atoms was mainly composed of a main pyridinic N centered at 398.0 eV and N–O bonding centered at 401.9 eV in the XPS N 1s spectrum [Fig. 3(c)]. The C/O and C/N ratios were 5.6 and 29.4, respectively, indicating that a large number of heteroatoms were introduced on the NPN surfaces. The surface atomic ratios were similar to the elemental analysis results, which showed that carbon, oxygen, and nitrogen contents were 77.2, 19.4, and 3.4 wt.%, respectively.

Porous properties of the NPNs were characterized by a nitrogen adsorption and desorption isotherm method. The shape of the isotherm curve of the NPNs is similar to the International Union of Pure and Applied Chemistry (IUPAC) Type-I shapes, suggesting that they have a microporous structure [Fig. 4(a)]. The specific surface area of the NPNs is 1522 m^2 g^{-1}, and the pore size distribution data shows that the NPNs mainly have nanometer-scale pores of ∼4 nm [Fig. 4(b)]. The pore volumes gradually increase with decreasing

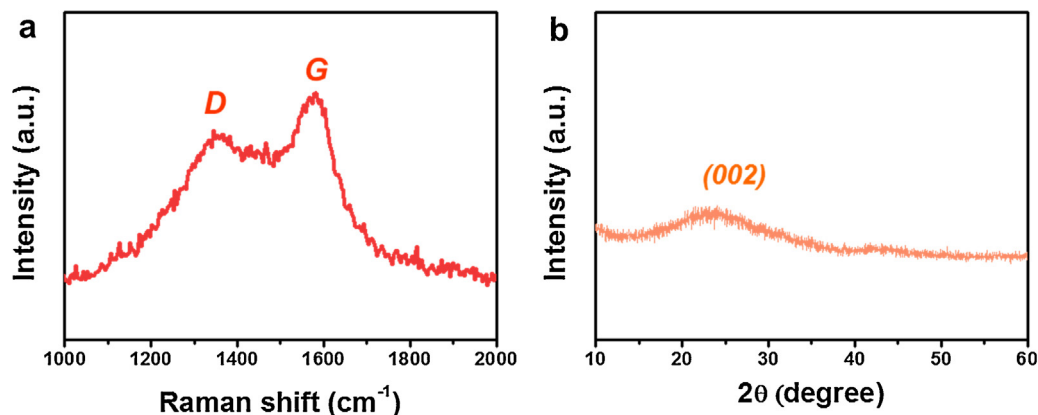**Fig. 2.** (a) Raman spectrum and (b) XRD pattern of NPNs.

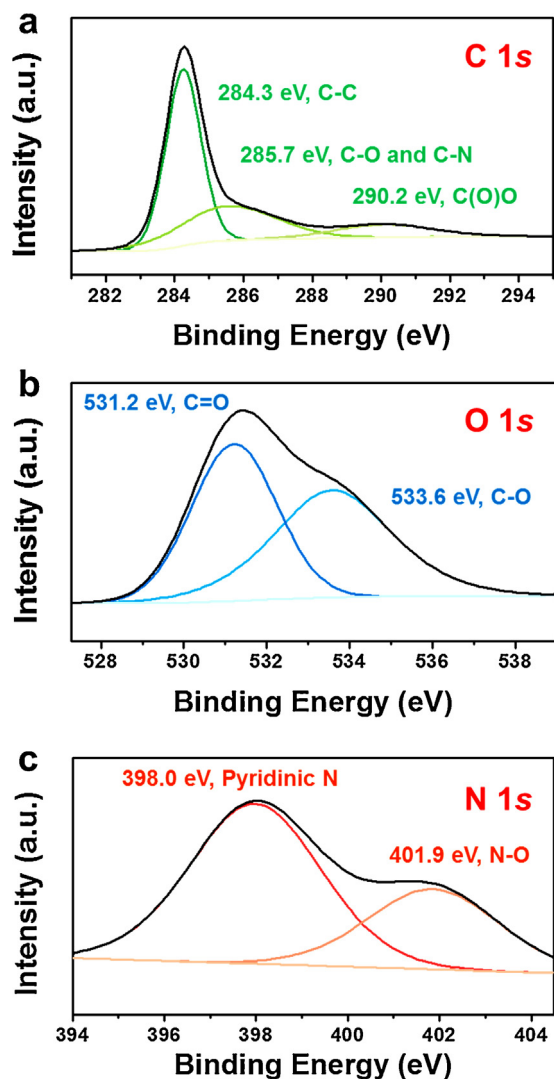**Fig. 3.** XPS C 1*s*, O 1*s*, and N 1*s* spectra of NPNs.

indicating nonmetallic behavior. At room temperature, the conductivity of the NPNs was 2.1×10^2 S cm^{-1} [Fig. 5(b)], at least 10-fold higher than that of reduced graphene oxide [29]. Nitrogen dopants could contribute to the high electrical conductivity by n-type doping effects [11].

The electrochemical performances of the NPNs were characterized in 6 M KOH aqueous electrolyte using a half-cell configuration with Ag/AgCl and Pt as the reference and counter electrodes, respectively, as shown in Fig. 6. The cyclovoltammograms of the NPNs were obtained over a potential range varying from −0.1 to −1.1 V vs. Ag/AgCl and showed a continuous increase in capacitance [Fig. 6(a)]. The steep slopes of the current changes at the switching potentials indicate a small mass-transfer resistance. The rectangular cyclovoltammograms gradually dented at higher scan rates, indicating an increase in mass-transfer resistance. Nevertheless, the initial shape of the cyclovoltammogram of the NPNs was maintained at the high scan rates. The commercial material Ketchen Black (KB), which has a specific surface area of 1286 m^2 g^{-1} and a mesoporous structure (Fig. S1), was used as the reference carbon material. The cyclovoltammograms of KB show a rectangular shape, even at the high scan rate of 100 mV s^{-1} [Fig. 6(b)]. However, the specific capacitance (*y*-axis scale) of KB is much smaller than that of the NPNs. The galvanostatic charge/discharge profiles of the NPNs show a triangular shape; however, the slope of the profile changed only slightly with decreasing voltage [Fig. 6(c)]. This change could have originated from a pseudocapacitive charge storage behavior on the redox-active heteroatoms [4,18,26,30], which coincides with the cyclovoltammogram, as shown in Fig. 6(a). Galvanostatic charge/discharge profiles of KB also show a triangular shape, indicating typical capacitive charge storage [Fig. 6(d)]. The specific capacitance of the NPNs is ∼330 F g^{-1} at 0.1 A g^{-1}, which is ∼2.7 times higher than that (122 F g^{-1}) of KBs [Fig. 6(e)]. Moreover, the capacitance is much higher than that of the previously reported results [7,9]. With increasing current density, the capacitance gradually decreased, and, at a high current density of 60 A g^{-1}, a specific capacitance of 221 F g^{-1} was maintained, which is still 2.2 times higher than that (∼100 F g^{-1}) of KB. The superior rate performances of the NPNs were further characterized by a Nyquist plot in the frequency range from 100 kHz to 0.1 Hz, as shown in Fig. 6(f). The plot features a transition between the RC semicircle and electrolyte migration. This corresponds to a resistance of 0.95 Ω, smaller than that (1.19 Ω) of KB. The diffusion resistance of the electrolyte ions is significantly small; therefore, the ESR of the NPNs is ∼0.98 Ω, which indicates easy accessibility of the pores to the electrolyte ions. In addition, the NPNs showed a significant cyclic performance over a series of 20,000 cycles [Fig. 7]; after 20,000 cycles, 85.6% of the initial capacitance was maintained.
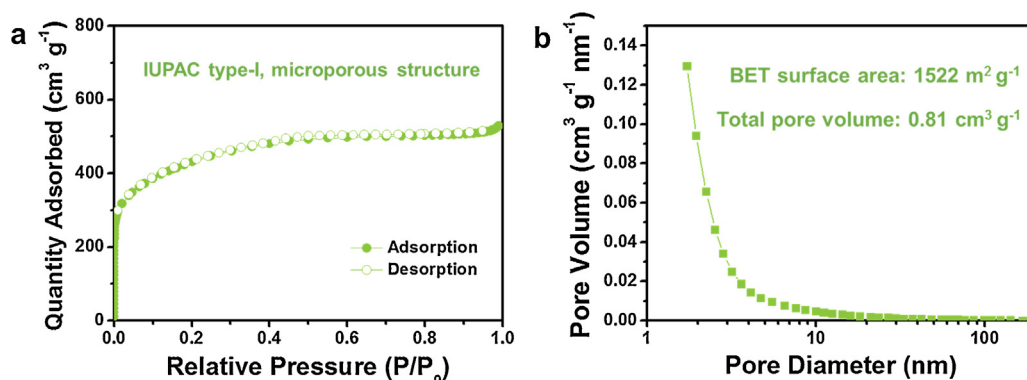
pore size, and the total pore volume was calculated as 0.81 cm^3 g^{-1}, as shown in Fig. 4(b). A highly functionalized and porous single NPN particle was transferred on the two-probe, as shown in Fig. 1(g), and its electrical properties were characterized [Fig. 5]. The current–voltage (*I*–*V*) plot was highly symmetric and linear throughout the different temperature regions. The conductivity, $\sigma(T)$, decreased with increasing temperature [Fig. 5(a)],

Fig. 4. (a) Nitrogen adsorption and desorption isotherm curves and (b) pore size distribution data of NPNs.
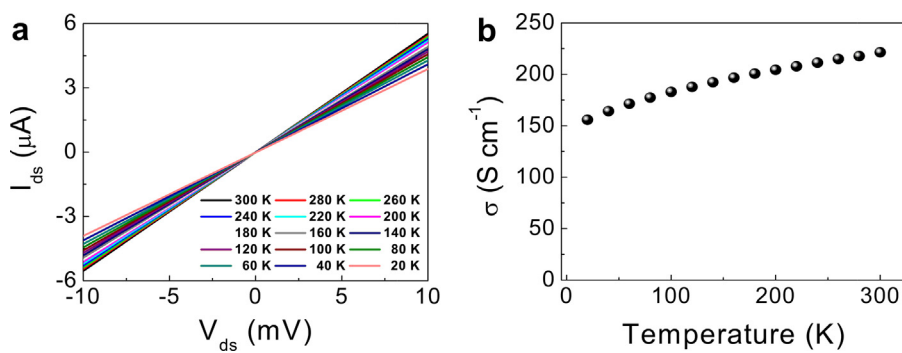
Fig. 5. (a) Temperature-dependent current–voltage (*I–V*) characteristics measured from 20 K to 300 K with a step of 20 K and (b) conductivity curve of the NPNs.
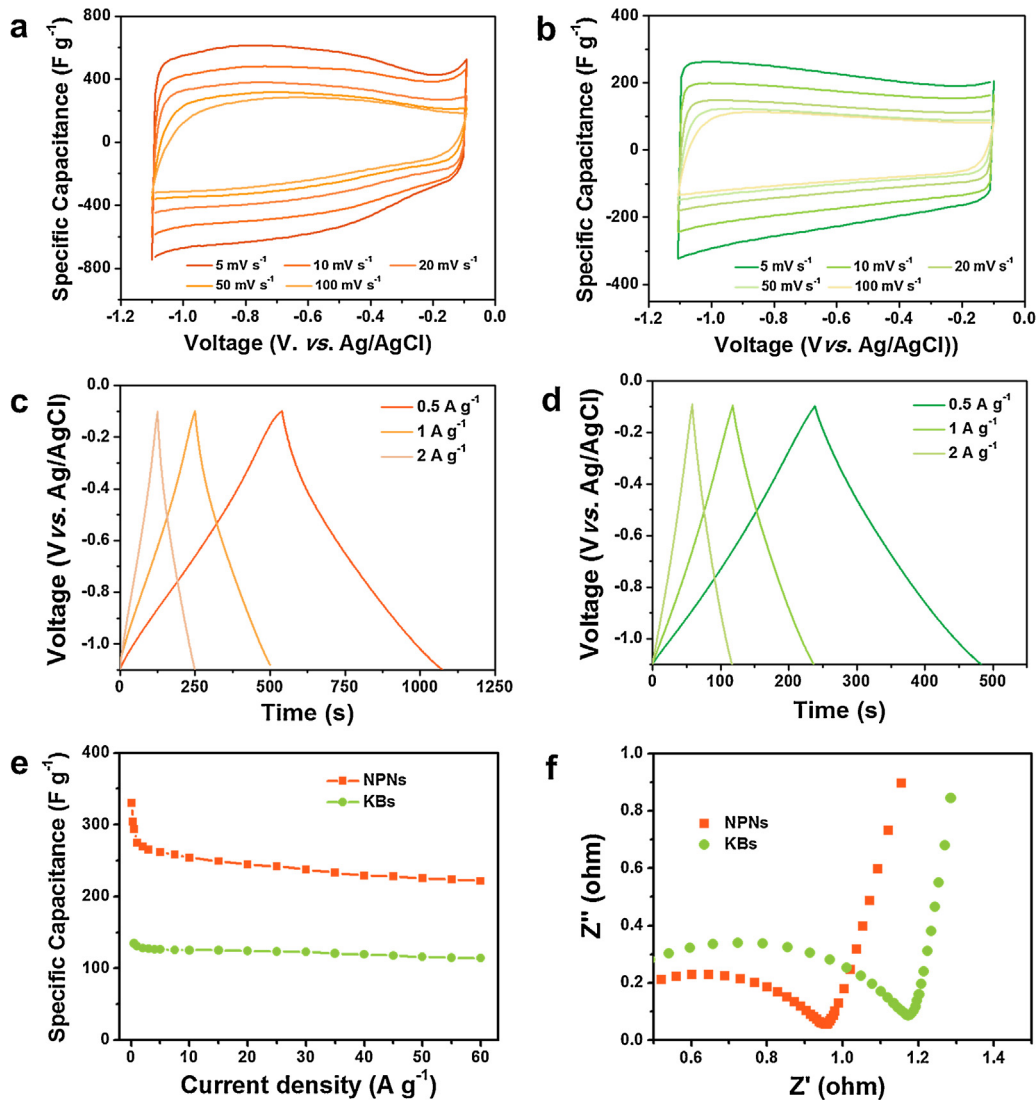

Fig. 6. Electrochemical performance results of NPNs over a voltage window of −0.1 to −1.1 V vs. Ag/AgCl in 6 M KOH. Cyclovoltammograms of (a) NPNs and (b) KB at various scan rates from 5 to 100 mV s^{-1}, galvanostatic charge/discharge profiles of (c) NPNs and (d) KB at different current densities, and (e) rate capabilities of NPNs and KB over a current density range of 0.1–60 A g^{-1}. (f) Nyquist plot of NPNs and KB in the frequency range from 100 kHz to 0.1 Hz.
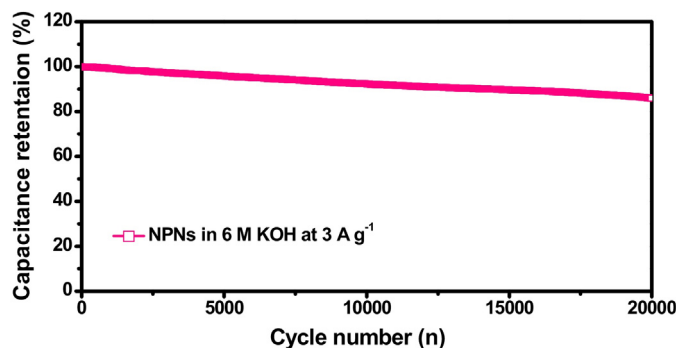
Fig. 7. Cyclic performance of the NPNs in a 6 M KOH aqueous electrolyte at a current density of 3 A g^{-1} for over 20,000 repetitive cycles.

Conclusion

In summary, NPNs were fabricated from Citreae peels by simple pyrolysis with potassium hydroxide followed by an acid treatment. The resulting NPNs had a 2D nanostructure with a high aspect ratio (>100) and a rough surface containing numerous nanometer-scale pores. In addition, the NPNs had a high specific surface area of 1522 m^2 g^{-1}, high electrical conductivity of 2.1 × 10^2 S cm^{-1}, and a large amount of oxygen (19.4 wt.%) and nitrogen (3.4 wt.%) heteroatoms. These outstanding material properties led to good electrochemical performance of the NPNs as electrodes for supercapacitors. The NPNs showed a high specific capacitance of 330 F g^{-1} at 0.1 A g^{-1}, and a specific capacitance of 221 F g^{-1} was maintained at a current density of 60 A g^{-1}, indicating a good rate capability. In addition, stable cycles were maintained for more than 20,000 charge/discharge cycles, in which capacitance retention was 85.6%.

Acknowledgments

Appendix A. Supplementary data

Supplementary data associated with this article can be found, in the online version, at doi:10.1016/j.jiec.2016.08.002.

References

[1] P. Simon, Y. Gogotsi, Nat. Mater. 7 (2008) 845–854.
[2] L.L. Zhang, X.S. Zhao, Chem. Soc. Rev. 38 (2009) 2520–2531.
[3] M. Lu, F. Béguin, E. Frackowiak (Eds.), Supercapacitors: Materials, Systems and Applications, John Wiley & Sons, 2013.
[4] Y.S. Yun, S.Y. Cho, J. Shim, B.H. Kim, S.-J. Chang, S.J. Baek, et al. Adv. Mater. 25 (2013) 1993–1998.
[5] H. Jiang, P.S. Lee, C. Li, Energy Environ. Sci. 6 (2013) 41–53.
[6] A.G. Pandolfo, A.F. Hollenkamp, J. Power Sources 157 (2006) 11–27.
[7] K. Xia, Q. Gao, J. Jiang, J. Hu, Carbon 46 (2008) 1718–1726.
[8] Y.S. Yun, C. Im, H.H. Park, I. Hwang, Y. Tak, H.-J. Jin, J. Power Sources 234 (2013) 285–291.
[9] E. Raymundo-Piñero, K. Kierzek, J. Machnikowski, F. Béguin, Carbon 44 (2006) 2498–2507.
[10] C. Liu, Z. Yu, D. Neff, A. Zhamu, B.Z. Jang, Nano Lett. 10 (2010) 4863–4868.
[11] Y.S. Yun, G. Yoon, K. Kang, H.-J. Jin, Carbon 80 (2014) 246–254.
[12] F. Picó, J.M. Rojo, M.L. Sanjuán, A. Ansón, A.M. Benito, M.A. Callejas, et al. J. Electrochem. Soc. 151 (2004) A831–A837.
[13] Y. Lv, F. Zhang, Y. Dou, Y. Zhai, J. Wnag, H. Liu, et al. J. Mater. Chem. 22 (2012) 93–99.
[14] Y.S. Yun, M.E. Lee, M.J. Joo, H.-J. Jin, J. Power Sources 246 (2014) 540–547.
[15] W. Xiong, M. Liu, L. Gan, Y. Lv, Y. Li, L. Yang, et al. J. Power Sources 196 (2011) 10461–10464.
[16] J. Li, X. Wang, Q. Huang, S. Gamboa, P.J. Sebastian, J. Power Sources 158 (2006) 784–788.
[17] M.D. Stoller, S. Park, Y. Zhu, J. An, R.S. Ruoff, Nano Lett. 8 (2008) 3498–3502.
[18] Y.S. Yun, S. Lee, N.R. Kim, M. Kang, C. Leal, K.-Y. Park, et al. J. Power Sources 313 (2016) 142–151.
[19] W. Wang, S. Guo, M. Penchev, I. Ruiz, K.N. Bozhilov, D. Yan, et al. Nano Energy 2 (2013) 294–303.
[20] F. Sun, J. Gao, X. Liu, X. Pi, Y. Yang, S. Wu, Appl. Surf. Sci. 387 (2016) 857–863.
[21] H. Zhang, O. Noonan, X. Huang, Y. Yang, C. Xu, L. Zhou, et al. ACS Nano 10 (2016) 4579–4586.
[22] K. Huang, M. Li, Z. Chen, Y. Yao, X. Yang, Electrochim. Acta 158 (2015) 306–313.
[23] D. Hulicova-Jurcakova, M. Kodama, S. Shiraishi, H. Hatori, Z.H. Zhu, G.Q. Lu, Adv. Funct. Mater. 19 (2009) 1800–1809.
[24] C.-M. Chen, Q. Zhang, M.-G. Yang, C.-H. Huang, Y.-G. Yang, M.-Z. Wang, Carbon 50 (2012) 3572–3584.
[25] Y.S. Yun, J. Shim, Y. Tak, H.-J. Jin, RSC Adv. 2 (2012) 4353–4358.
[26] Y.S. Yun, H.H. Park, H.-J. Jin, Materials 5 (2012) 1258–1266.
[27] S.Y. Cho, Y.S. Yun, S. Lee, D. Jang, K.-Y. Park, J.K. Kim, et al. Nat. Commun. 6 (2015) 7145.
[28] J. Romanos, M. Beckner, T. Rash, L. Firlej, B. Kuchta, P. Yu, et al. Nanotechnology 23 (2012) 015401.
[29] Y.S. Yun, V.-D. Le, H. Kim, S.-J. Chang, S.J. Baek, S. Park, et al. J. Power Sources 262 (2014) 79–85.
[30] Y.S. Yun, S.Y. Cho, H.-J. Jin, Macromol. Res. 22 (2014) 509–514.